Particuology 53 (2020) 58–62

Contents lists available at ScienceDirect

Particuology

journal homepage: www.elsevier.com/locate/partic

Short communication

Efficient coating fabrication of onion-like carbon nanoparticles via aerosol deposition

Yaoyao Fu[a,b], Yi Liu[a], Hua Li[a,*]

[a] Key Laboratory of Marine Materials and Related Technologies, Zhejiang Key Laboratory of Marine Materials and Protective Technologies, Ningbo Institute of Materials Technology and Engineering, Chinese Academy of Sciences, Ningbo 315201, China
[b] Center of Materials Science and Optoelectronics Engineering, University of Chinese Academy of Sciences, Beijing 100049, China

ARTICLE INFO

Article history:
Received 25 February 2019
Received in revised form
17 November 2019
Accepted 8 January 2020
Available online 4 March 2020

Keywords:
Onion-like carbon
Aerosol deposition
Nanoparticles
Thick film
Particle deformation

ABSTRACT

In this work, an onion-like carbon (OLC) nanoparticle coating with a micron-sized thickness was fabricated via aerosol deposition (AD). During the room temperature impact consolidation (RTIC), the OLC nanoparticles (5–10 nm) experienced remarkable deformation along both the perpendicular and parallel directions to the coating-substrate interface. Particle deformation, mechanical interlocking, and van der Waals forces between the OLC particles were revealed as the major regimes for coating formation. The aerosol deposition technique might open new avenues for fabricating carbonaceous nanostructures for various functional applications.

Introduction

Studies reporting the synthesis of diverse carbonaceous nanomaterials have triggered growing global research efforts exploring their versatile applications. Among the carbonaceous nanomaterials, onion-like carbon (OLC) was first discovered by Iijima (1980) and further studied by Ugarte (1992). Typically, OLC particles have the attributes of spherical contours, several concentric sp^2 graphene-like carbon shells, controllable surface properties, high conductivities, and a nanoscopic size, which endows them with extensive potential applications in various fields, such as lubrication (Berman et al., 2018), energy (Xue et al., 2017), environmental remediation (Ko et al., 2016), biomedical engineering (Ghosh, Sonkar, Saxena, & Sarkar, 2011), and electronics (Yang, Zhang, & Kim, 2016). Particularly, heat treatment of detonation nanodiamond has enabled the large-scale fabrication of OLC particles (Makgopa, Raju, Ejikeme, & Ozoemena, 2017; Szerencsi & Radnoczi, 2009), which has facilitated practical research using these particles. Regardless of the advancements made on the synthesis and application of OLCs, designing and controlling their agglomeration in different dimensions and size scales remain a challenge. Therefore, it is of great significance to explore the possibility of obtaining OLC nanostructures from the nano to macroscale.

In previous studies, OLC coatings have been fabricated via ion injection (Cabioch, Riviere, & Delafond, 1995), chemical vapor deposition (CVD) (Zhang et al., 2012), electromagnetically accelerated plasma spraying (Gubarevich et al., 2003), and electrophoretic deposition (Pech et al., 2010). However, the structural homogeneity, chemical purity, and fabrication efficiency of these methods are poor. To develop new synthetic routes, maintaining the intrinsic physicochemical properties of zero-dimensional OLC nanoparticles is essential. Aerosol deposition (AD), also referred to as vacuum cold spray (VCS), is a room temperature impact consolidation (RTIC) process that has shown viability for depositing nanomaterial functional films and coatings (Liu, Dang, Wang, Huang, & Li, 2014; Wang, Sung, & Kim, 2015). In this work, the AD technique was employed to fabricate an OLC nanostructured coating, and the deposition mechanism of the OLC nanoparticles were elucidated.

OLC coating deposition

Commercially available OLC nanoparticles (Nafortis Co., Ltd., China) fabricated via detonation nanodiamonds were used with additional purification and heat treatment; they had a size of 5–10 nm in diameter with typical concentric carbon atom rings, and a spacing of 0.34 nm between successive cages can be clearly

* Corresponding author.
E-mail address: lihua@nimte.ac.cn (H. Li).

https://doi.org/10.1016/j.partic.2020.01.001

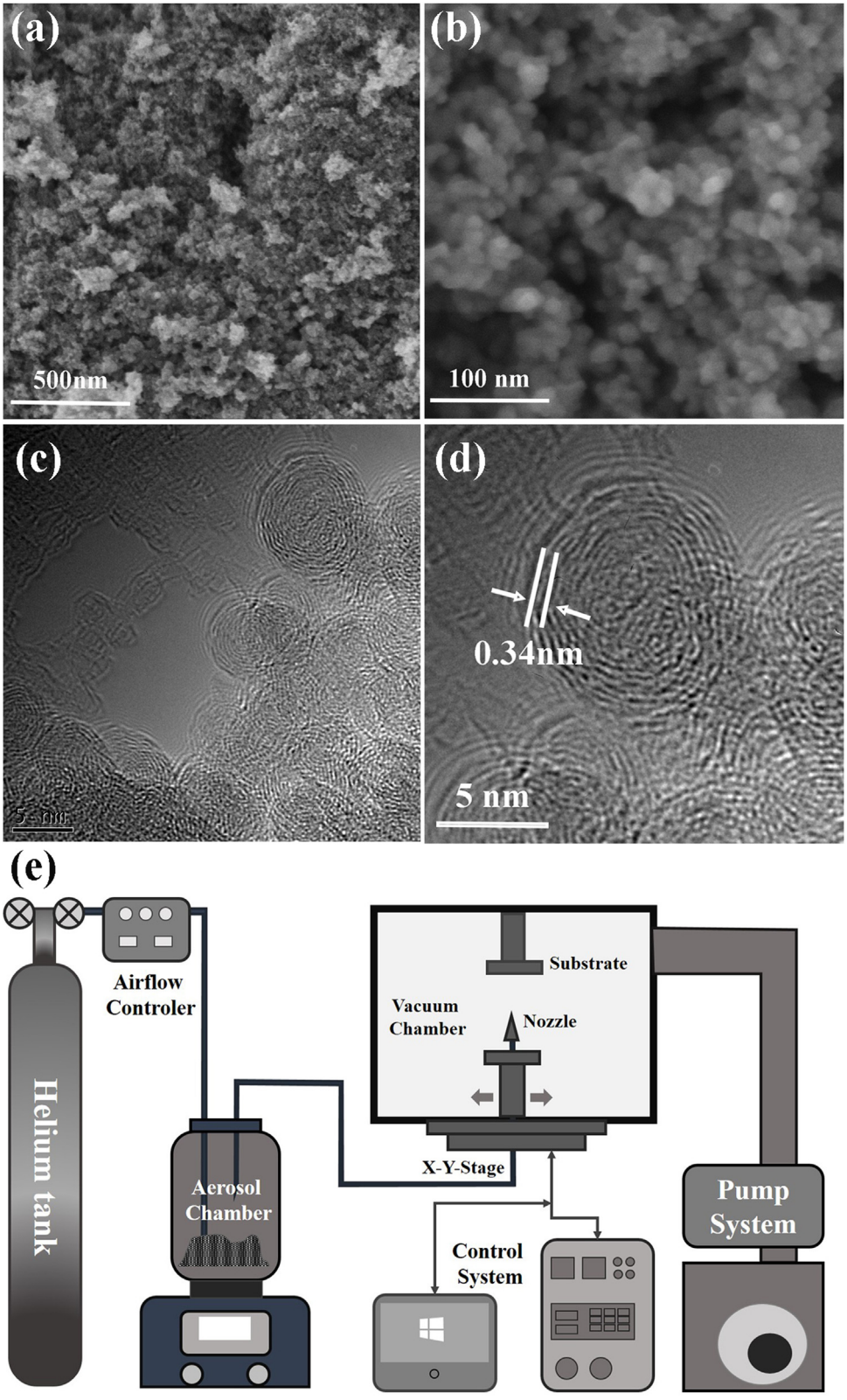

Fig. 1. Morphology of the OLC particles and diagram of the AD system, (a, b) SEM image of the OLC nanoparticles, (c, d) TEM image of the OLC nanoparticles showing typical onion-like concentric carbon atom rings, and (e) schematic diagram of the AD deposition system.

observed (Fig. 1(a)–(d)). The OLC coatings were deposited via an AD process operated at room temperature and silicon wafers were used as the substrates. The homemade AD system (Xi'an Jiaotong University, China) comprised a vacuum chamber, a set of rotary and root pumps, an aerosol generation room, an accelerating carrier gas unit, and a control unit (Fig. 1(e)). The deposition chamber contained a substrate holder and a micron-sized nozzle integrated with a three-dimensional worktable. For spraying, a primary rotary

vane vacuum pump coupled to a mechanical booster was used to pump down the chamber to ~2000 Pa and a secondary roots vacuum pump was used to reach ~20 Pa. Helium gas with a flow rate of 5 L/min was used for feeding and accelerating the powder feedstock. The ultrafine OLC powder was agitated and accelerated via the carrier gas through the micro-orifice Laval nozzle. For the AD deposition process, the distance between the nozzle and substrate was fixed at 10 mm, and the scanning speed of the nozzle was fixed at 10 mm/s.

Results and discussion

Coating microstructure

OLC nanostructured coatings were successfully fabricated via the AD process, as schematically shown in Fig. 1(d). To the best of our knowledge, this is the first time that OLC nanoparticles were consolidated to form nanostructured coatings at room temperature. The cross-sectional SEM view of the as-deposited OLC coating shows a porous topographical morphology (Fig. 2(a)), and the coating had a thickness of ~12 μm.

The chemistry of the as-received OLC nanoparticles was further characterized via Raman spectroscopy (Fig. 2(b)) prior to coating formation. The Raman spectrum of the OLC nanoparticles shows clear D-/G-mode peaks of partially-graphitic carbon located at 1337 cm^{-1} and a pronounced range of overtones and combinational modes at 1581 cm^{-1}. The 2D peak at ~2677 cm^{-1} is activated via double-resonance of photons at the K-point in the Brillouin zone (Zeiger, Jackel, Asian, Weingarth, & Presser, 2015). The coatings show almost identical Raman peaks compared with the starting OLC nanoparticles (Fig. 2(b)), which indicates that the chemical characteristics of OLC were retained after the coating process. The surface SEM image (Fig. 2(c)) of the coating show a consistent porous structure with the cross-sectional (Fig. 2(a)) and magnified

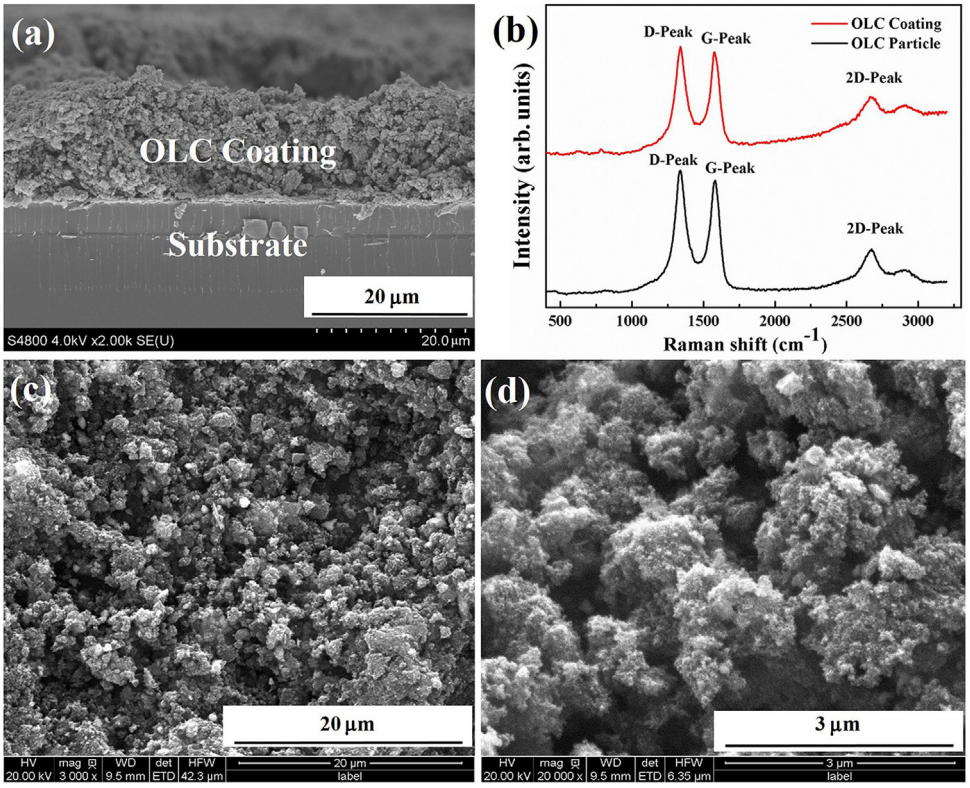

Fig. 2. Characterization of the as-deposited OLC coating, (a) cross-sectional FESEM image of the OLC coating, (b) Raman spectra of the starting OLC particles and the coatings, (c, d) typical surface topographical FESEM surface images of the OLC coatings.

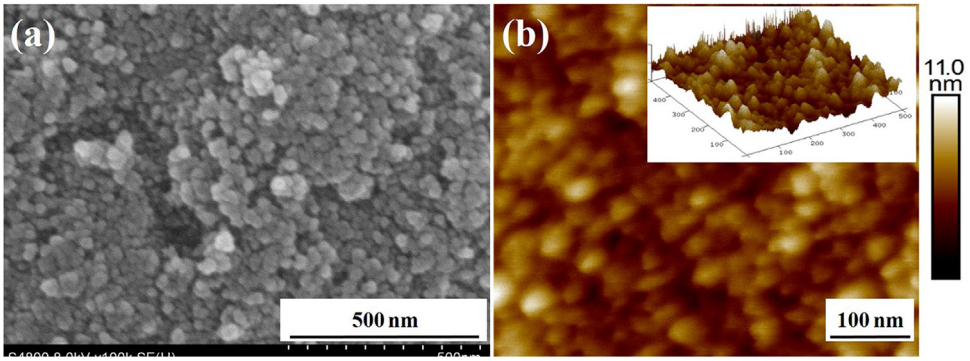

Fig. 3. Characteristics of the subsurface microstructure of the as-deposited OLC coating, (a) FESEM image showing the subsurface morphology of the OLC coating, and (b) AFM 2D and 3D images showing the tight stacking of the OLC nanoparticles at the subsurface of the coating.

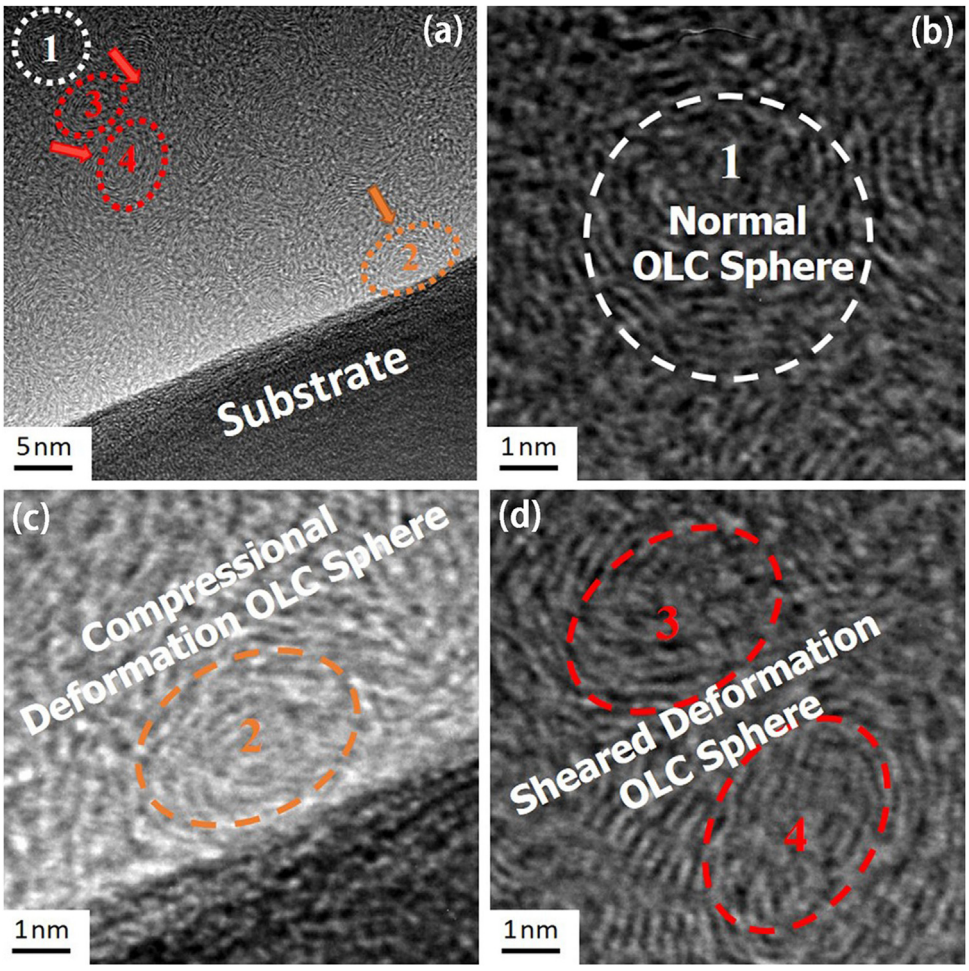

Fig. 4. HRTEM images of the OLC coating deposited on a silicon wafer showing its cross-sectional morphology (a–d), the images shown in (b–d) are magnified ones of the selected areas in (a). The highlighted areas are non-deformed OLC particle (1), and deformed OLC particles (2–4) in the coating.

SEM images indicating aggregation of the OLC particles during the coating formation stage (Fig. 2(d)).

Room temperature impact consolidation

To further characterize the subsurface microstructure of the coating, its top thin layer was repeatedly exfoliated using adhesive tape. Interestingly, it can be noted that the fresh subsurface of the coating clearly shows tight stacking of the OLC nanoparticles (Fig. 3(a)). Further AFM examination (Fig. 3(b)) reveals that the individual OLC nanoparticles agglomerate, forming particle clusters that could be recognized via SEM imaging. A large difference could be observed between the morphology of the coating/substrate (Fig. 3) and coating/atmosphere (Fig. 2), which indicated that there was high cohesion between the coating/substrate and low cohesion between coating/atmosphere.

Because no heating or melting was involved during the AD process, it is believed that RTIC is essential for impact coating formation during AD of nanoparticles. For the AD coating deposition, the initial plastic deformation followed by RTIC of the sprayed particles are key steps for coating formation (Akedo, 2008). Our previous work indicated that graphene stays in the coating as the first layer, intimately contacting with the substrate and its curvature changes during the AD process (Liu, Dang et al., 2014; Liu, Huang, & Li, 2014). In this case, RTIC can be clearly evidenced by the consolidated OLC nanoparticle clusters seen in the coating (Fig. 3(a), (b)).

Coating formation mechanism

The RTIC phenomenon was also verified via cross-sectional TEM characterization of the coating (Fig. 4). The starting OLC nanoparticles display a normal spherical shape (Fig. 1(c), (d)), after the coating deposition, they turn to show a refined structure. Strikingly, deformation of the OLC nanoparticles can be observed in the coating (Fig. 4(c), (d)), particularly at the regions close to the substrate-coating interface. The transformation from a sphere to an oval clearly indicates that the nanoparticles experienced significant impact along the vertical direction during the AD process. This is likely caused by the bombardment of successively arriving particles on the previously settled ones during the coating formation process. It has been reported that some fullerene-like inorganic nanoparticles are capable of deforming and recovering to their original shape (Lahouij et al., 2012). Additionally, in this case, deformation of the OLC particles other than perpendicularly to the substrate surface could also be seen (Fig. 4(d)), suggesting that shearing of the particles also occurred during the RTIC process. Shearing has already been reported for ceramic particles during the AD coating process (Assadi, Gartner, Stoltenhoff, & Kreye, 2003), presumably because ceramics have a limited ability for plastic deformation.

Previous studies have established that the RTIC effect is primarily responsible for mechanical interlocking of the nanoparticles during AD deposition (Akedo, 2008). Because of the presence of RTIC and the two forms of particle deformation, the particles

bombard each other, which facilitates mechanical interlocking.

For the OLC coating, the distance between adjacent OLC particles (distance between the outermost carbon cage of two adjacent particles) was determined to be ~0.34 nm (Fig. 4(c), (d)), which is close to the theoretical distance between each carbon wall. This suggests that apart from the mechanical interlocking and electrostatic interaction between the OLC particles, van der Waals forces also play an important role in the formation of the OLC coatings.

Conclusion

In summary, the fabrication of an OLC nanostructured coating was realized via aerosol deposition and the particles retained their original physicochemical characteristics after the coating process. Room temperature impact consolidation resulted in a remarkable deformation of the OLC nanoparticles, and mechanical interlocking and van der Waals interaction played crucial roles in the coating formation process. The results provide insights for the large-scale fabrication of carbonaceous nanostructures for versatile functional applications via the AD route.

Conflict of interest

The authors declare that they have no conflict of interest.

Acknowledgements

This work was supported by the National Natural Science Foundation of China (grant # 41476064 and 31500772) and Zhejiang Provincial Natural Science Foundation of China (LY18C100003). The authors would also like to thank Professor Changjiu Li's group in Xi'an Jiaotong University, China for technical assistance in aerosol deposition.

References

Akedo, J. (2008). Room temperature impact consolidation (RTIC) of fine ceramic powder by aerosol deposition method and applications to microdevices. *Journal of Thermal Spray Technology*, *17*(2), 181–198.

Assadi, H., Gartner, F., Stoltenhoff, T., & Kreye, H. (2003). Bonding mechanism in cold gas spraying. *Acta Materialia*, *51*(15), 4379–4394.

Berman, D., Narayanan, B., Cherukara, M. J., Sankaranarayanan, S., Erdemir, A., Zinovev, A., et al. (2018). Operando tribochemical formation of onion-like-carbon leads to macroscale superlubricity. *Nature Communication*, *9*(1), 1164.

Cabioch, T., Riviere, J. P., & Delafond, J. (1995). A new technique for fullerene onion formation. *Journal of Materials Science*, *30*(19), 4787–4792.

Ghosh, M., Sonkar, S. K., Saxena, M., & Sarkar, S. (2011). Carbon nano-onions for imaging the life cycle of drosophila melanogaster. *Small*, *7*(22), 3170–3177.

Gubarevich, A. V., Kitamura, J., Usuba, S., Yokoi, H., Kakudate, Y., & Odawara, O. (2003). Onion-like carbon deposition by plasma spraying of nanodiamonds. *Carbon*, *41*(13), 2601–2606.

Iijima, S. (1980). Direct observation of the tetrahedral bonding in graphitized carbon-black by high-resolution electron-microscopy. *Journal of Crystal Growth*, *50*(3), 675–683.

Ko, Y. J., Choi, K., Lee, S., Cho, J. M., Choi, H. J., Hong, S. W., et al. (2016). Chromate adsorption mechanism on nanodiamond-derived onion-like carbon. *Journal of Hazardous Materials*, *320*, 368–375.

Lahouij, I., Bucholz, E. W., Vacher, B., Sinnott, S. B., Martin, J. M., & Dassenoy, F. (2012). Lubrication mechanisms of hollow-core inorganic fullerene-like nanoparticles: Coupling experimental and computational works. *Nanotechnology*, *23*(37), 1–10.

Liu, Y., Huang, J., & Li, H. (2014). Nanostructural characteristics of vacuum cold-sprayed hydroxyapatite/graphene-nanosheet coatings for biomedical applications. *Journal of Thermal Spray Technology*, *23*(7), 1149–1156.

Liu, Y., Dang, Z., Wang, Y., Huang, J., & Li, H. (2014). Hydroxyapatite/graphene-nanosheet composite coatings deposited by vacuum cold spraying for biomedical applications: Inherited nanostructures and enhanced properties. *Carbon*, *67*, 250–259.

Makgopa, K., Raju, K., Ejikeme, P. M., & Ozoemena, K. I. (2017). High-performance Mn_3O_4/onion-like carbon (OLC) nanohybrid pseudocapacitor: Unravelling the intrinsic properties of OLC against other carbon supports. *Carbon*, *117*, 20–32.

Pech, D., Brunet, M., Durou, H., Huang, P., Mochalin, V., Gogotsi, Y., et al. (2010). Ultrahigh-power micrometre-sized supercapacitors based on onion-like carbon. *Nature Nanotechnology*, *5*(9), 651–654.

Szerencsi, M., & Radnoczi, G. (2009). The mechanism of growth and decay of carbon nano-onions formed by ordering of amorphous particles. *Vacuum*, *84*(1), 197–201.

Ugarte, D. (1992). Curling and closure of graphitic networks under electron-beam irradiation. *Nature*, *359*(6397), 707–709.

Wang, C., Sung, H. K., & Kim, N. Y. (2015). Aerosol deposition-based micropatterning of barium titanate via sulphur hexafluoride inductively coupled plasma etching. *Vacuum*, *114*, 49–53.

Xue, G., Xu, Y., Ding, T., Li, J., Yin, J., Fei, W., et al. (2017). Water-evaporation-induced electricity with nanostructured carbon materials. *Nature Nanotechnology*, *12*(4), 317–321.

Yang, J., Zhang, Y., & Kim, D. Y. (2016). Electrochemical sensing performance of nanodiamond-derived carbon nano-onions: Comparison with multiwalled carbon nanotubes, graphite nanoflakes, and glassy carbon. *Carbon*, *98*, 74–82.

Zeiger, M., Jackel, N., Asian, M., Weingarth, D., & Presser, V. (2015). Understanding structure and porosity of nanodiamond-derived carbon onions. *Carbon*, *84*, 584–598.

Zhang, C., Li, J., Liu, E., He, C., Shi, C., Du, X., et al. (2012). Synthesis of hollow carbon nano-onions and their use for electrochemical hydrogen storage. *Carbon*, *50*(10), 3513–3521.